Report Documentation Page		*Form Approved* *OMB No. 0704-0188*

Public reporting burden for the collection of information is estimated to average 1 hour per response, including the time for reviewing instructions, searching existing data sources, gathering and maintaining the data needed, and completing and reviewing the collection of information. Send comments regarding this burden estimate or any other aspect of this collection of information, including suggestions for reducing this burden, to Washington Headquarters Services, Directorate for Information Operations and Reports, 1215 Jefferson Davis Highway, Suite 1204, Arlington VA 22202-4302. Respondents should be aware that notwithstanding any other provision of law, no person shall be subject to a penalty for failing to comply with a collection of information if it does not display a currently valid OMB control number.

1. REPORT DATE **18 APR 2013**	2. REPORT TYPE	3. DATES COVERED **00-00-2013 to 00-00-2013**
4. TITLE AND SUBTITLE **Imaging moving objects from multiply scattered waves and multiple sensors**		5a. CONTRACT NUMBER
		5b. GRANT NUMBER
		5c. PROGRAM ELEMENT NUMBER
6. AUTHOR(S)		5d. PROJECT NUMBER
		5e. TASK NUMBER
		5f. WORK UNIT NUMBER
7. PERFORMING ORGANIZATION NAME(S) AND ADDRESS(ES) **Air Force Research Laboratory,Sensors Directorate,Dayton,OH,45433**		8. PERFORMING ORGANIZATION REPORT NUMBER
9. SPONSORING/MONITORING AGENCY NAME(S) AND ADDRESS(ES)		10. SPONSOR/MONITOR'S ACRONYM(S)
		11. SPONSOR/MONITOR'S REPORT NUMBER(S)

12. DISTRIBUTION/AVAILABILITY STATEMENT **Approved for public release; distribution unlimited**

13. SUPPLEMENTARY NOTES

14. ABSTRACT

In this paper, we develop a linearized imaging theory that combines the spatial, temporal and spectral components of multiply scattered waves as they scatter from moving objects. In particular, we consider the case of multiple fixed sensors transmitting and receiving information from multiply scattered waves. We use a priori information about the multipath background. We use a simple model for multiple scattering, namely scattering from a fixed, perfectly reflecting (mirror) plane. We base our image reconstruction and velocity estimation technique on a modification of a filtered backprojection method that produces a phase-space image. We plot examples of point-spread functions for different geometries and waveforms, and from these plots, we estimate the resolution in space and velocity. Through this analysis, we are able to identify how the imaging system depends on parameters such as bandwidth and number of sensors. We ultimately show that enhanced phase-space resolution for a distribution of moving and stationary targets in a multipath environment may be achieved using multiple sensors.

15. SUBJECT TERMS					
16. SECURITY CLASSIFICATION OF:			17. LIMITATION OF ABSTRACT **Same as Report (SAR)**	18. NUMBER OF PAGES **15**	19a. NAME OF RESPONSIBLE PERSON
a. REPORT **unclassified**	b. ABSTRACT **unclassified**	c. THIS PAGE **unclassified**			

Imaging moving objects from multiply scattered waves and multiple sensors

Analee Miranda[1] and Margaret Cheney[2,3]

[1] Sensors Directorate, Air Force Research Laboratory, Dayton, OH 45433, USA
[2] Department of Mathematics, Colorado State University, Fort Collins, CO 80523-1874, USA
[3] Department of Electrical and Computer Engineering, Colorado State University, Fort Collins, CO 80523-1874, USA

E-mail: analee.miranda@wpafb.af.mil and cheney@math.colostate.edu

Abstract

In this paper, we develop a linearized imaging theory that combines the spatial, temporal and spectral components of multiply scattered waves as they scatter from moving objects. In particular, we consider the case of multiple fixed sensors transmitting and receiving information from multiply scattered waves. We use *a priori* information about the multipath background. We use a simple model for multiple scattering, namely scattering from a fixed, perfectly reflecting (mirror) plane. We base our image reconstruction and velocity estimation technique on a modification of a filtered backprojection method that produces a phase-space image. We plot examples of point-spread functions for different geometries and waveforms, and from these plots, we estimate the resolution in space and velocity. Through this analysis, we are able to identify how the imaging system depends on parameters such as bandwidth and number of sensors. We ultimately show that enhanced phase-space resolution for a distribution of moving and stationary targets in a multipath environment may be achieved using multiple sensors.

(Some figures may appear in colour only in the online journal)

1. Introduction

Traditional wave-based imaging theory makes the assumption that the waves travel directly from the sensor to the target and back. However, there are many situations in practice where complicated scenes cause waves to multiply scatter from non-target objects in the scene of interest. This makes imaging targets of interest more difficult because of the additional unknowns that are introduced. A number of researchers have considered wave-based imaging in the presence of multipathing when the scene of interest consists of stationary targets illuminated by waves transmitted from moving platforms. The studies [9] and [4] showed that a backprojection algorithm that exploits multiply scattered fields can improve image fidelity if it is possible to uniquely identify the part of the data corresponding to each scattering

wave path. In particular, this work showed that targets oriented in certain directions can be effectively invisible from direct scattering but may become visible when multipath scattering is used in the image formation process. The studies [2] and [5] showed that, compared to standard backprojection, a backprojection algorithm that exploits multiply scattered fields can improve image resolution even if a method for *a priori* separating paths in the data is not feasible. This paper derives a data model, based on [1], that includes the effect of multiply scattered waves on moving targets and then develops a corresponding phase-space imaging method that accounts for multiple scattering in the data. We consider the case in which multiple sensors interrogate a distribution of moving targets that are restricted to a horizontal plane. We model multiple scattering with a perfectly reflecting (mirror) horizontal plane.

This geometry might arise in a variety of physical problems, including ultrasound, microwave tomography, seismic prospecting, and radar and sonar imaging. The perfect reflecting mirror is a simple model for the ocean surface, for example, that must be considered in marine seismic surveys, active sonar surveys and radar imaging in marine environments. Alternatively, the mirror could represent a reflecting surface in ultrasound, microwave tomography or radar imaging. In the discussion below, we use radar terminology, but the theory applies equally well to other modalities.

The mathematical model is discussed in section 2. Imaging is addressed in section 3, which outlines the backprojection-type algorithm for forming phase-space images, and then proceeds to analyze the corresponding point-spread function (PSF). Section 4 outlines simulations. Many of the details can be found in [6] and short summaries can be found in [7] and [8].

2. Mathematical data model

A radar receiver collects information from an electromagnetic wave that was sent from a transmitting antenna and that subsequently scattered off a set of (stationary or) moving targets in a scene. In this work, we assume that the scattered waves arrive at the radar receiver via multiple paths.

We assume that the electromagnetic field propagates in the lower half-space $\Omega = \{(x_1, x_2, x_3) \,|\, x_1, x_2 \in \mathbb{R}, x_3 < z_0\}$. The perfectly reflecting mirror is located at $\partial\Omega = \{(x_1, x_2, x_3) \,|\, x_1, x_2 \in \mathbb{R}, x_3 = z_0\}$. We denote the reflection of Ω with respect to $\partial\Omega$ by Ω^*.

Both Ω and Ω^* consist of a homogeneous, isotropic medium in which the wave propagation speed is c. The geometry is shown in figure 1.

We make the assumption that one component ψ of the electromagnetic field satisfies

$$\left(\nabla^2 - c^{-2}\partial_t^2 - V(t, \tilde{\boldsymbol{x}})\,\partial_t^2\right)\psi(t, \tilde{\boldsymbol{x}}, \boldsymbol{y}) = s(t - t_y, \tilde{\boldsymbol{x}}, \boldsymbol{y}), \tag{1}$$

with the boundary condition

$$\psi(t, \tilde{\boldsymbol{x}}, \boldsymbol{y})|_{\tilde{\boldsymbol{x}} \in \partial\Omega} = 0. \tag{2}$$

In order to define $V(t, \tilde{\boldsymbol{x}})$, consider first an object located at position $\tilde{\boldsymbol{x}}$ that moves with velocity $\boldsymbol{v}$. This object would be described by an index-of-refraction distribution with a parameter $\boldsymbol{v}$:

$$V_{\boldsymbol{v}}(t, \tilde{\boldsymbol{x}}) = c^{-2}\left[n_{\boldsymbol{v}}^2(\tilde{\boldsymbol{x}} - \boldsymbol{v}t) - 1\right]. \tag{3}$$

Multiple objects translating with the same velocity $\boldsymbol{v}$ can also be described in the form (3); for example, multiple cars moving along a highway at the same constant velocity $\boldsymbol{v}$ could be described by (3) in which $n_{\boldsymbol{v}}$ consists of multiple bumps, each bump representing one car. For objects translating with velocity $\boldsymbol{v}$, we write $q_{\boldsymbol{v}}(\tilde{\boldsymbol{x}}) = c^{-2}[n_{\boldsymbol{v}}^2(\tilde{\boldsymbol{x}}) - 1]$.
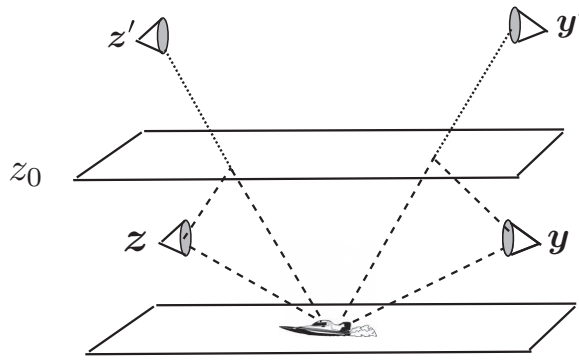
Figure 1. This shows the geometry with one transmitter at *y* and one receiver at *z*. The mirror is located at height z_0.

Objects moving with a different velocity can be described by an expression of the form (3) in which the velocity *v* is different. To describe two-way traffic along a highway, for example, *V* might be of the form

$$V(t, \tilde{x}) = c^{-2}\big[n_v^2(\tilde{x} - vt) - 1\big] + c^{-2}\big[n_{-v}^2(\tilde{x} + vt) - 1\big], \tag{4}$$

where n_v describes the cars moving in one direction and n_{-v} describes the cars moving with the same speed in the opposite direction.

If there are many objects moving with different velocities, then we can describe the distribution of multiple moving objects as

$$V(t, \tilde{x}) = \int c^{-2} q_v^2(\tilde{x} - vt)\, \mathrm{d}v. \tag{5}$$

We see that $q_v(\tilde{x})$ can be considered a scattering density in phase space.

2.1. Incident field

The *incident* field ψ^{in} is the field, propagating in the empty reflecting environment, that emanates from a transmitting antenna located at position *y*. The field ψ^{in} satisfies

$$(\nabla^2 - c^{-2}\partial_t^2)\psi^{\mathrm{in}} = \delta(\tilde{x} - y)s(t - t_y) \tag{6}$$

$$\psi^{\mathrm{in}}\big(t, \tilde{x}, y\big)\,|_{\partial\Omega} = 0. \tag{7}$$

An expression for the incident field ψ^{in} can be derived by using the method of images. Corresponding to the source location $y \in \Omega$, we define the virtual source at $y' = (y_1, y_2, 2z_0 - y_3)$.

First, the outgoing Green's function satisfying

$$(\nabla^2 - c^{-2}\partial_t^2)g(t, \tilde{x}, y) = \delta(\tilde{x} - y)\delta(t) \tag{8}$$

$$g|_{\partial\Omega} = 0 \tag{9}$$

is

$$g(t, \tilde{x}, y) = g_y(t, \tilde{x}, y) - g_{y'}(t, \tilde{x}, y), \tag{10}$$

where g_y is the free-space Green's function with a source at *y*:

$$g_y(t, \tilde{x}, y) = \frac{\delta\big(t - \frac{|\tilde{x} - y|}{c}\big)}{4\pi|\tilde{x} - y|} \tag{11}$$

3

and similarly $g_{y'}$ is the free-space Green's function with a virtual source at y'. Note that g vanishes at the boundary $\partial\Omega$.

This means that the solution to (6) with (7) is

$$
\psi^{\text{in}}(t, \tilde{x}, y) = -\int g(t - T, \tilde{x})\delta(\tilde{x} - y)s(T - t_y)\,dy\,dT
$$

$$
= \frac{s\left(t - t_y - \frac{|\tilde{x}-y'|}{c}\right)}{4\pi|\tilde{x} - y'|} - \frac{s\left(t - t_y - \frac{|\tilde{x}-y|}{c}\right)}{4\pi|\tilde{x} - y|}. \tag{12}
$$

2.2. Scattered field

We split the field into the incident field ψ^{in} and the scattered field ψ^{sc}:

$$
\psi = \psi^{\text{in}} + \psi^{\text{sc}}. \tag{13}
$$

We subtract (6) from (1) and use (13) to arrive at the partial differential equation for the scattered field:

$$
\left(\nabla^2 - c^{-2}\partial_t^2\right)\psi^{\text{sc}}(t, z, y) = V(t, \tilde{x})\partial_t^2\psi^{\text{sc}}(t, z, y)
$$
$$
\psi^{\text{sc}}|_{\partial\Omega} = 0. \tag{14}
$$

We use the *Born* or *single-scattering* approximation [1], replacing ψ^{sc} on the right side of (14) by ψ^{in}. The corresponding solution of (14), measured at the receiver y, constitutes the data d. With the Green function (10), we obtain

$$
d(t, y, z) = \int \left(\frac{\delta\left(t - t' - \frac{|\tilde{z}-\tilde{x}|}{c}\right)}{4\pi|\tilde{z} - \tilde{x}|} - \frac{\delta\left(t - t' - \frac{|\tilde{z}'-\tilde{x}|}{c}\right)}{4\pi|\tilde{z}' - \tilde{x}|}\right) V(t', \tilde{x})\partial_t^2\psi^{\text{in}}(t', \tilde{x}, y)\,dt'\,d\tilde{x}
$$

$$
= \int \frac{\delta\left(t - t' - \frac{|\tilde{z}-\tilde{x}|}{c}\right)}{4\pi|\tilde{z} - \tilde{x}|}\int q_v\left(\tilde{x} - vt'\right)d\tilde{v}\,\frac{\ddot{s}_y\left(t' - t_y - \frac{|\tilde{x}-y|}{c}\right)}{4\pi|\tilde{x} - y|}\,dt'\,d\tilde{x}
$$

$$
- \int \frac{\delta\left(t - t' - \frac{|\tilde{z}-\tilde{x}|}{c}\right)}{4\pi|\tilde{z} - \tilde{x}|}\int q_v\left(\tilde{x} - vt'\right)d\tilde{v}\,\frac{\ddot{s}_y\left(t' - t_y - \frac{|\tilde{x}-y'|}{c}\right)}{4\pi|\tilde{x} - y'|}\,dt'\,d\tilde{x}
$$

$$
- \int \frac{\delta\left(t - t' - \frac{|\tilde{z}'-\tilde{x}|}{c}\right)}{4\pi|\tilde{z}' - \tilde{x}|}\int q_v\left(\tilde{x} - vt'\right)d\tilde{v}\,\frac{\ddot{s}_y\left(t' - t_y - \frac{|\tilde{x}-y|}{c}\right)}{4\pi|\tilde{x} - y|}\,dt'\,d\tilde{x}
$$

$$
+ \int \frac{\delta\left(t - t' - \frac{|\tilde{z}'-\tilde{x}|}{c}\right)}{4\pi|\tilde{z}' - \tilde{x}|}\int q_v\left(\tilde{x} - vt'\right)d\tilde{v}\,\frac{\ddot{s}_y\left(t' - t_y - \frac{|\tilde{x}-y'|}{c}\right)}{4\pi|\tilde{x} - y'|}\,dt'\,d\tilde{x}. \tag{15}
$$

Equation (15) yields a model for the scattered wavefield. Each term of (15) has a clear physical interpretation. The first term (line 2) corresponds to activating the transmitter at y with a waveform s_y, starting at time t_y. This activation results in a wave leaving the transmitter and propagating directly to the target, arriving at time t'. The moving target that at time t' is located at $\tilde{x}$ was, at time $t = 0$, located at $\tilde{x} - vt'$. The current density induced on the target by the incident field is assumed to be proportional to the second derivative of the transmitted signal; this is a result of the Born approximation. After interaction with the target, the wave then propagates directly from $\tilde{x}$ to $\tilde{z}$.

The second term of (15) (line 3) corresponds again to activating the transmitter at y with the waveform s_y. This time, however, the wave reflects from the mirror on its way to the target; by the method of images, the field that arrives is the negative of the same wave traveling in

free space but transmitted from the virtual location y'. This field interacts with the target and propagates to the receiver as before.

The third term of (15) (line 4) corresponds to direct-path propagation between the transmitter and the target, and a reflection from the mirror on the way to the receiver; by the method of images, the received wave is the negative of the wave propagating in free space that would have been received at the virtual receiver location z'. The fourth term corresponds to mirror reflections between the target and both the transmitter and receiver.

We interchange the order of integration and perform a change of variables $x = \tilde{x} - vt'$:

$$
\begin{aligned}
d(t, y, z) = & \int \frac{\delta\left(t - t' - \frac{|x+vt'-z|}{c}\right)}{4\pi |x + vt' - z|} \int q_v(x) \frac{\ddot{s}_y\left(t' - t_y - \frac{|x+vt'-y|}{c}\right)}{4\pi |x + vt' - y|} \, dt' \, dx \, dv \\
& - \int \frac{\delta\left(t - t' - \frac{|x+vt'-z|}{c}\right)}{4\pi |x + vt' - z|} \int q_v(x) \frac{\ddot{s}_y\left(t' - t_y - \frac{|x+vt'-y'|}{c}\right)}{4\pi |x + vt' - y'|} \, dt' \, dx \, dv \\
& - \int \frac{\delta\left(t - t' - \frac{|x+vt'-z'|}{c}\right)}{4\pi |x + vt' - z'|} \int q_v(x) \frac{\ddot{s}_y\left(t' - t_y - \frac{|x+vt'-y|}{c}\right)}{4\pi |x + vt' - y|} \, dt' \, dx \, dv \\
& + \int \frac{\delta\left(t - t' - \frac{|x+vt'-z'|}{c}\right)}{4\pi |x + vt' - z'|} \int q_v(x) \frac{\ddot{s}_y\left(t' - t_y - \frac{|x+vt'-y'|}{c}\right)}{4\pi |x + vt' - y'|} \, dt' \, dx \, dv. \quad (16)
\end{aligned}
$$

Finally, we carry out the t' integration in (16) by using properties of delta functions with more complicated arguments as in [6]. In particular, in the first term of (15) (line 2), for example, we find that the delta function contributes only to t' satisfying

$$
0 = t - t' - \frac{|x + vt' - z|}{c}. \quad (17)
$$

This time we denote t' by $\bar{t}_{xz}$. We also introduce the notation $R_{x,y}(\bar{t}_{xz}) = |x + v\bar{t}_{xz} - z|$ and $\mu = |f'_{xz}(\bar{t}_{xz}(t))|$ for $f'_{xz}(t') = -1 - \hat{R}_{xz}(t')/c$.

This leads to the general data set for a single source y,

$$
\begin{aligned}
d(t, z, y) = & \int \frac{\ddot{s}_y[\bar{t}_{xz}(t) - t_y - \frac{R_{xy}(\bar{t}_{xz}(t))}{c}] q_v(x)}{(4\pi)^2 R_{xz}(\bar{t}_{xz}(t)) R_{xy}(\bar{t}_{xz}(t)) \mu_{xz,v}(t)} \, dx \, dv \\
& - \int \frac{\ddot{s}_y[\bar{t}_{xz}(t) - t_y - \frac{R_{xy'}(\bar{t}_{xz}(t))}{c}] q_v(x)}{(4\pi)^2 R_{xz}(\bar{t}_{xz}(t)) R_{xy'}(\bar{t}_{xz}(t)) \mu_{xz,v}(t)} \, dx \, dv \\
& - \int \frac{\ddot{s}_y[\bar{t}_{xz'}(t) - t_y - \frac{R_{xy}(\bar{t}_{xz'}(t))}{c}] q_v(x)}{(4\pi)^2 R_{xz'}(\bar{t}_{xz'}(t)) R_{xy}(\bar{t}_{xz'}(t)) \mu_{xz',v}(t)} \, dx \, dv \\
& + \int \frac{\ddot{s}_y[\bar{t}_{xz'}(t) - t_y - \frac{R_{xy'}(\bar{t}_{xz'}(t))}{c}] q_v(x)}{(4\pi)^2 R_{xz'}(\bar{t}_{xz'}(t)) R_{xy'}(\bar{t}_{xz'}(t)) \mu_{xz',v}(t)} \, dx \, dv. \quad (18)
\end{aligned}
$$

2.3. Slow-moving approximation

We consider only objects that move significantly slower than the speed of light. Consequently, we assume that the distance traveled by the objects during the relevant time is much smaller than the distances between the targets and the transmitters and receivers. Specifically, we assume

$$
|v|t, \ |v|^2 t^2 \omega_{\max}/c \ \ll \ |x - z|, \ |x - z'|, \ |x - y|, \ |x - y'|, \quad (19)
$$

where $\omega_{\max}$ is the effective maximum angular frequency of the signal s_y.

This means that a first-order Taylor approximation may be made such that

$$R_{xz}(t) = |z - x + vt| = R_{xz}(0) + \widehat{R}_{xz}(0) \cdot vt + O\left(\frac{|v|^2}{R_{xz}}\right), \tag{20}$$

where, $R_{xz}(0) = x - z$, $R_{xz}(0) = |R_{xz}(0)|$, and $\widehat{R}_{xz}(0) = \frac{R_{xz}(0)}{R_{xz}(0)}$.

The techniques of [3] can be used to derive a time dilation or a Doppler scale factor

$$\alpha_{xvyz} = \frac{1 - \frac{\hat{R}_{xy}(0) \cdot v}{c}}{1 + \frac{\hat{R}_{xz}(0) \cdot v}{c}} \tag{21}$$

that is closely related to the Doppler shift. We can further approximate this factor as

$$\alpha_{xvyz} \cong 1 - (\hat{R}_{xy}(0) + \hat{R}_{xz}(0)) \cdot \frac{v}{c}. \tag{22}$$

We immediately see that the Doppler scale factor α_{xvyx} depends on the bisector $(\hat{R}_{xy}(0) + \hat{R}_{xz}(0))$.

With the approximations (20) and notation (21), the data expression (18) for the slow-mover case becomes

$$\begin{aligned}
d_s(z, y, t) = &\int \frac{\ddot{s}_y[\alpha_{xvyz} \cdot \left(t - \frac{R_{xz}(0)}{c}\right) - \frac{R_{xy}(0)}{c} - t_y] q_v(x)}{(4\pi)^2 R_{xz}(0) R_{xy}(0) \mu_{xz,v}} \, dx \, dv \\
&- \int \frac{\ddot{s}_y[\alpha_{xvy'z} \cdot \left(t - \frac{R_{xz}(0)}{c}\right) - \frac{R_{xy'}(0)}{c} - t_y] q_v(x)}{(4\pi)^2 R_{xz}(0) R_{xy'}(0) \mu_{xz,v}} \, dx \, dv \\
&- \int \frac{\ddot{s}_y[\alpha_{xvyz'} \cdot \left(t - \frac{R_{xz'}(0)}{c}\right) - \frac{R_{xy}(0)}{c} - t_y] q_v(x)}{(4\pi)^2 R_{xz'}(0) R_{xy}(0) \mu_{xz',v}} \, dx \, dv \\
&+ \int \frac{\ddot{s}_y[\alpha_{xvy'z'} \cdot \left(t - \frac{R_{xz'}(0)}{c}\right) - \frac{R_{xy'}(0)}{c} - t_y] q_v(x)}{(4\pi)^2 R_{xz'}(0) R_{xy'}(0) \mu_{xz',v}} \, dx \, dv.
\end{aligned} \tag{23}$$

In order to more succinctly describe the data model, we write

$$R_{xy} \equiv R_{x10}, \qquad R_{xy'} \equiv R_{x20,} \qquad R_{xz} \equiv R_{x01}, \qquad R_{xz'} \equiv R_{x02}. \tag{24}$$

In other words, we use the subscripts xjk and vjk as placeholders for the dependence on the object, receiver or transmitter location. A zero is added in the respective placeholder if there is no dependence on a transmitter and/or receiver. Moreover, we use $j, k = 1$ for the actual sensors and $j, k = 2$ for the virtual sensors. We also write $\alpha_{v,y,z'}$ as α_{v12}, etc.

With this notation, we rewrite equation (23):

$$d_s(z, y, t) = \int \sum_{j,k=1}^{2} \Upsilon_s^{jk} q_v(x) \, dx \, dv, \tag{25}$$

where

$$\Upsilon_s^{jk} = \frac{(-1)^{j+k} \ddot{s}[\alpha_{xvjk}\left(t - \frac{R_{x0k}(0)}{c}\right) - \frac{R_{xj0}(0)}{c} - t_y]}{(4\pi)^2 R_{x0k}(0) R_{xj0}(0) \mu_{x0k,v}}. \tag{26}$$

2.4. Narrowband waveform

Most radars use narrowband waveforms, which may be written as $s(t) = a(t) e^{-i\omega_{0j0}t}$, where $a(t)$ is slowly varying and ω_{0j0} is the carrier frequency for the transmitter y. (Note that in

keeping with the notation defined above, the zeros indicate that there is no object or receiver dependence.)

$$d_N(z, y, t) = \sum_{j,k=1}^{2} \int \left(\frac{\omega_{0j0}}{4\pi}\right)^2 (-1)^{j+k} \frac{\exp\left(-i\omega_{0j0}[\alpha_{xvjk}\left(t - \frac{R_{x0k}(0)}{c}\right) - \frac{R_{xj0}(0)}{c} - t_y]\right)}{R_{x0k}(0) R_{xj0}(0) \mu_{x0k,v}}$$
$$\times a\left(t - t_y - \frac{R_{x0k}(0) + R_{xj0}(0)}{c}\right) q_v(x) \, dx \, dv. \tag{27}$$

where we use the approximation $\alpha_{vjk} = 1$ in the slowly varying amplitude a. Substituting the time-independent exponential phase terms into the function $\varphi_{xvjk} = \frac{\omega_{0j0}}{c}[R_{xj0}(0) + \alpha_{vjk}R_{x0k}(0) + ct_y]$, we rewrite (27) as

$$d_N(z, y, t) = \sum_{j,k=1}^{2} \int \left(\frac{\omega_{0j0}}{4\pi}\right)^2 (-1)^{j+k} \frac{e^{i\varphi_{xvjk}}e^{-i\omega_{xj0}\alpha_{vjk}t}}{R_{xj0}(0) R_{x0k}(0) \mu_{x0k,v}}$$
$$\times a\left(t - t_y - \frac{R_{x0k}(0) - R_{xj0}(0)}{c}\right) q_v(x) \, dx \, dv$$
$$= \sum_{j,k=1}^{2} (-1)^{j+k} \, d_N^{jk}(t, z). \tag{28}$$

3. Image reconstruction

In this section, we first describe how we form an image. Then we describe how we analyze the reconstructed image. We test our analysis by performing numerical experiments. We conclude with a summary of our results.

3.1. Image formation

The approach we take to form an image of our simulated data involves applying a matched filter or filtered adjoint to the data. From the data $d(t, z, y)$, we form an image $I(p, u)$ of the objects with hypothesized velocity u, that, at time $t = 0$, are located at position p.

Consider, for example, the case where the transmitters and receivers illuminate only one path, say the direct path. In this case, the data are simply

$$d_N^{11}(t, z, y) = [\mathcal{P}^{11}q_v(x)](t, z, y) = \int \Upsilon_N^{11}(x, v, t, z, y)q_v(x) \, dx \, dv, \tag{29}$$

where we have applied (19), (20) and the narrowband approximation to (26) to obtain $\Upsilon_N^{11}(x, v, t, z, y)$:

$$\Upsilon_N^{11}(x, v, t, z, y) = \left(\frac{\omega_y}{4\pi}\right)^2 \frac{e^{i\varphi_{xyz}}e^{-i\omega_y\alpha_{vyz}t}}{R_{xz}(0) R_{xz}(0) \mu_{xz,v}} a_{11}\left(t - t_y - \frac{R_{xz}(0) - R_{xy}(0)}{c}\right). \tag{30}$$

In order to form an image $I(p, u)$ at position p and velocity u, we apply the adjoint operator to $d_N^{11}(t, z, y)$:

$$I(p, u) = \mathcal{P}^{11*}d_N^{11}$$
$$= \sum_{z,y} \int \Upsilon_N^{11*}(p, u, t, z, y) \, d_N^{11}(t, z, y) \, dt$$
$$= \int \sum_{z,y} \Upsilon_N^{11*}(p, u, t, z, y) \Upsilon_N^{11}(x, v, t, z, y) \, dt \, q_v(x) \, dx \, dv$$
$$= \int \mathcal{K}_N^{11}(p, x, u, v) q_v(x) \, dx \, dv, \tag{31}$$

where the kernel

$$\mathcal{K}_N^{11}(\boldsymbol{p}, \boldsymbol{x}, \boldsymbol{u}, \boldsymbol{v}) = \int \sum_{z,y} \Upsilon_N^{11*}(\boldsymbol{p}, \boldsymbol{u}, t, z, \boldsymbol{y}) \Upsilon_N^{11}(\boldsymbol{x}, \boldsymbol{v}, t, z, \boldsymbol{y}) \, \mathrm{d}t \tag{32}$$

is the *PSF* for the imaging system. We note that the PSF and the corresponding image are in general complex-valued. The Cauchy–Schwartz inequality implies that the integral kernel (32) is maximized when $(\boldsymbol{p}, \boldsymbol{u}) = (\boldsymbol{x}, \boldsymbol{v})$. In particular, each term is bounded in magnitude by

$$\left| \int \Upsilon_N^{11*}(\boldsymbol{p}, \boldsymbol{u}, t, \ldots) \Upsilon_N^{11}(\boldsymbol{x}, \boldsymbol{v}, t, \ldots) \, \mathrm{d}t \right| \leqslant \|\Upsilon_N^{11*}(\boldsymbol{p}, \boldsymbol{u}, \ldots)\|_2 \|\Upsilon_N^{11}(\boldsymbol{x}, \boldsymbol{v}, \ldots)\|_2, \tag{33}$$

where $\|\Upsilon(\ldots)\|_2 = (\int |\Upsilon(\ldots, t, \ldots)|^2 \, \mathrm{d}t)^{1/2}$, and equality is attained in (33) when $\Upsilon_N^{11}(\boldsymbol{p}, \boldsymbol{u}, t, z, \boldsymbol{y}) = \Upsilon_N^{11}(\boldsymbol{x}, \boldsymbol{v}, t, z, \boldsymbol{y})$. This occurs when $(\boldsymbol{p}, \boldsymbol{u}) = (\boldsymbol{x}, \boldsymbol{v})$.

If we can identify the parts of the data that correspond to the different paths, then we can form separate images for each path and coherently (or noncoherently) add the resulting images:

$$I(\boldsymbol{p}, \boldsymbol{u}) = \sum_{i,j} \mathcal{P}^{ij*} d^{ij}. \tag{34}$$

If it is not possible to distinguish paths, then the data are of the form $d = \sum_{l,m} d^{lm}$, we apply the adjoint operator $\mathcal{P}_N^* = \sum_{i,j} \mathcal{P}_N^{ij*}$ to form an image:

$$\begin{aligned} I(\boldsymbol{p}, \boldsymbol{u}) &= \mathcal{P}_N^* \, \mathrm{d}_N(\boldsymbol{y}, z, t) \\ &= \int \sum_{z,y} \Upsilon_N^*(\boldsymbol{p}, \boldsymbol{u}, t, z, \boldsymbol{y}) \Upsilon_N(\boldsymbol{x}, \boldsymbol{v}, t, z, \boldsymbol{y}) \, \mathrm{d}t q_v(\boldsymbol{x}) \, \mathrm{d}\boldsymbol{x} \, \mathrm{d}\boldsymbol{v}, \end{aligned} \tag{35}$$

where the subscript N denotes the narrowband slowly moving case. The image that is formed gives us an approximation to the true reflectivity function $\boldsymbol{q}_v(\boldsymbol{x})$, added to copies of $\boldsymbol{q}_v$ in the wrong location.

3.2. Image analysis

In order to analyze the image in the case when data from the different paths cannot be separated, we need to investigate the relationship between the image and the true reflectivity $\boldsymbol{q}_v(\boldsymbol{x})$.

To do this, we use (28) in (35). The result is

$$I(\boldsymbol{p}, \boldsymbol{u}) = \sum_{j,k=1}^{2} (-1)^{j+k} K_N^{jk}(\boldsymbol{p}, \boldsymbol{u}; \boldsymbol{x}, \boldsymbol{v}) \boldsymbol{q}_v(\boldsymbol{x}) \, \mathrm{d}\boldsymbol{x} \, \mathrm{d}\boldsymbol{v}, \tag{36}$$

where the sum of all K_N^{jk} terms is the PSF for this imaging system. Each K_N^{jk} is given by

$$\begin{aligned} K_N^{jk}(\boldsymbol{p}, \boldsymbol{x}, \boldsymbol{u}, \boldsymbol{v}) = -\int \omega_{0j0}^2 a_{jk}^* &\left(t - t_y - \frac{(R_{p0k}(0) + R_{pj0}(0))}{c} \right) \\ \times a_{jk} &\left(t - t_y - \frac{(R_{x0k}(0) + R_{xj0}(0))}{c} \right) \\ \times \mathrm{e}^{-\mathrm{i}\varphi_{pjk}} \mathrm{e}^{\mathrm{i}\omega_{0j0}\alpha_{pjk}} &\mathrm{e}^{\mathrm{i}\varphi_{xjk}} \mathrm{e}^{-\mathrm{i}\omega_{0j0}\alpha_{xjk}} \frac{R_{p0k}(0) R_{pj0} \mu_{p0k,\boldsymbol{u}}}{R_{x0k}(0) R_{xj0} \mu_{x0k,\boldsymbol{u}}} \, \mathrm{d}t. \end{aligned} \tag{37}$$

Equation (37) can be further simplified by noting

$$\begin{aligned} \varphi_{xvjk} - \varphi_{pujk} \quad &= \frac{\omega_{0j0}}{c}[R_{xj0}(0) - \alpha_{vjk}R_{x0k}(0) + ct_y - (R_{pj0}(0) - \alpha_{ujk}R_{p0k}(0) + ct_y)] \\ &= \frac{\omega_{0j0}}{c}[R_{xj0}(0) - R_{pj0}(0) - \alpha_{vjk}R_{x0k}(0) + \alpha_{ujk}R_{p0k}(0)] \\ &= \frac{\omega_{0j0}}{c}[R_{xj0}(0) - R_{pj0}(0) - (1 + \beta_{vjk})R_{x0k}(0) + (1 + \beta_{ujk})R_{p0k}(0)] \\ &= \frac{\omega_{0j0}}{c}[c\triangle\tau_{xpjk} - \beta_{vjk}R_{x0k}(0) + \beta_{ujk}R_{p0k}(0)], \end{aligned} \tag{38}$$

8

where

$$\triangle\tau_{xpjk} = \frac{R_{xj0}(0) - R_{pj0}(0) - R_{x0k}(0) + R_{p0k}(0)}{c}. \tag{39}$$

With this notation, we can write (37) as

$$K_N^{jk}(\boldsymbol{p}, \boldsymbol{u}; \boldsymbol{x}, \boldsymbol{v}) = \int \omega_{0j0}^2 A_{jk}(\omega_{0j0}[\beta_{pjk} - \beta_{xjk}], \triangle\tau_{xpjk}) \exp\left(i\omega_{0j0}[\beta_{pjk} - \beta_{xjk}]\left[\frac{R_{xj0}(0)}{c} - t_y\right]\right)$$

$$\times \exp\left(\frac{-i\omega_{0j0}\beta_{pjk}}{c}[R_{xj0}(0) - R_{pj0}(0)]\right) \frac{R_{p0k}(0)R_{pj0}(0)\mu_{p0k,\boldsymbol{u}}}{R_{x0k}(0)R_{xj0}(0)\mu_{x0k,\boldsymbol{u}}} \, dt, \tag{40}$$

where $\alpha_{vyz} \approx 1 + \beta_{vyz}$ (see equation (22)) and

$$A(\tilde{\omega}, \tau) = e^{-i\omega_0\tau} \int a^*(t - \tau)a(t)\, e^{i\tilde{\omega}t} \, dt \tag{41}$$

is the well-known narrowband ambiguity function [10].

We recall that the ambiguity function characterizes the ability of a given waveform to provide range and (down-range) velocity information. Thus, formulas (36) and (40) provide a way to examine the performance of a system for imaging moving targets in terms of the sensor locations and the waveforms they transmit. These formulas thus provide a theoretical basis for the allocation of radar resources.

4. Numerical examples

In this section, we provide some numerical examples that show how the number of sensors affects the image reconstruction of a stationary and a moving target. We analyze the resolution of the data by plotting a PSF, which is equivalent to an image of a single point-like target. All simulations used the following parameters.

(i) *Target*. The target is a single point-like scatterer located in the horizontal plane. For the stationary target images, the true target is located at $\boldsymbol{x} = (25\text{ m}, 25\text{ m})$ in a scene in which the x axis runs from 0 to 50 m and the y axis runs from 0 to 50 m. For the moving target images, the target is located at (35 m, 35 m) in a scene where both x and y axes run from 0 to 70 m.

(ii) *Waveform*. Each sensor transmitted a known stepped-frequency waveform with 218 pulses stepping through the frequencies of 30–40 GHz uniformly. Alternatively, this can be thought of as a signal with a 35 GHz center frequency and a 10 GHz bandwidth.

(iii) *Sensor geometry*. The sensors lie around the scene of interest. See figure 2 for the exact placement. Note: the velocity plots use only the nine transmitters and one receiver set-up.

(iv) *Reflector*. The reflector was a perfectly reflecting mirror situated 100 m above the scene of interest. The location of the reflector is assumed to be known.

In all cases, the images are spatial images. The units on both the horizontal and vertical axes are in meters.

Figures 3 and 4 show reconstructions of a stationary target; figure 3 shows the case in which we are able to identify the part of the received signal coming from different transmitters, whereas figure 4 shows the case in which we do not have this information. All the images in figures 3 and 4 show the spatial image at velocity $(0, 0)$.

We note that since figure 3 is reconstructed using prior information about the location of the reflecting mirror, and consequently the wave path is known, there are no multipath ambiguities because the algorithm matches the correct time delay with the correct path.

As we increase the number of sensors, the resolution improves: the red region corresponding to the target is thinner than the backprojection ellipses. Since each image
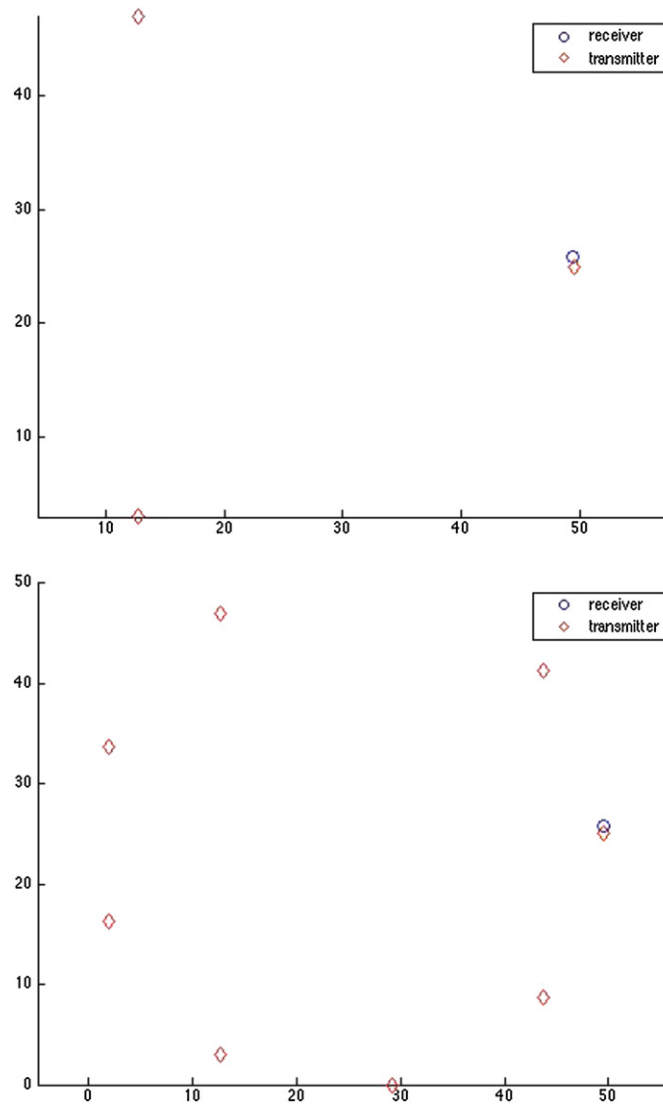
Figure 2. Geometry of the sensor placement. Top image: three transmitters and one receiver. Bottom image: nine transmitters and one receiver.

cell represents 2 m of physical distance, we estimate the resolution for the stationary point target in this example to be about 2 m.

In figure 4, on the other hand, the image is reconstructed without the knowledge of the paths traveled by different parts of the received signal. As the figure shows, multipath artifacts now appear. We note that there is a relationship between the configuration of the sensor positions and the artifacts. Adding more sensors diminishes the artifacts.

In figure 5, the target was moving with velocity $(3, 3) \times 10 \, \mathrm{m \, s^{-1}}$. Figure 5 shows spatial images at two different velocity hypotheses, the velocity $(1, 3) \times 10 \, \mathrm{m \, s^{-1}}$ (top) and the correct velocity (bottom). The numerical examples presented in this paper are only a representative subset of velocity images. The reader is referred to [6] for a larger set of velocity images. We
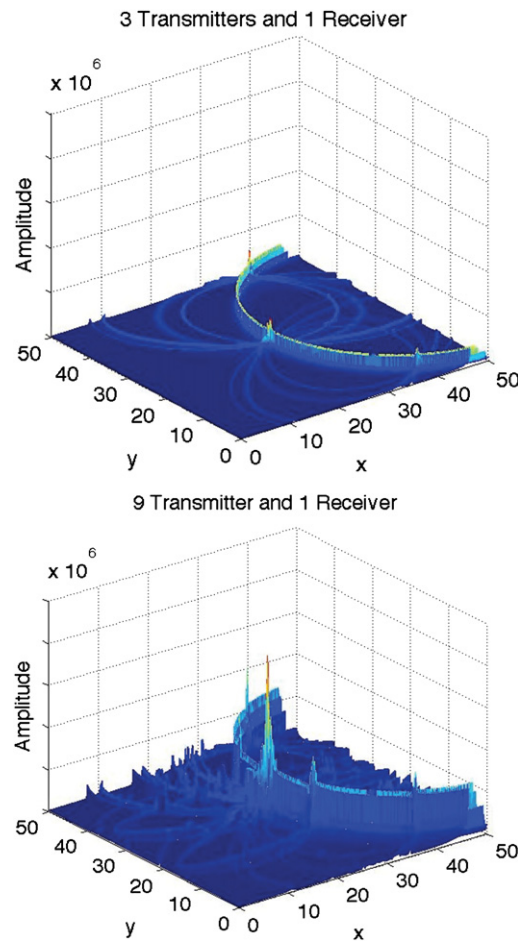
Figure 3. Stationary object PSF—perfect reflector, known paths. Top image: three transmitters and one receiver. Bottom image: nine transmitters and one receiver. The vertical scale (image amplitude) is the same for both plots.

can determine the correct velocity by choosing the image with the best target focus. In this way, we may use our modified backprojection method to estimate the velocity of a moving target. In figure 5, we show that if we use *a priori* information about the geolocation of a target, then we may estimate that target's velocity by examining the four-dimensional PSF. As we see in figure 5, the target is geolocated with the best resolution at the correct velocity $(3, 3) \times 10$ m s^{-1}. At the incorrect velocity, the true target disappears and artifacts appear at the wrong locations.

From our velocity sampling, we estimate the resolution in velocity to be about 10 m s^{-1}, and the image shows the spatial resolution to be about 3 m. In this case, the waveform we used provided better spatial resolution than velocity resolution. A waveform with better Doppler resolution would provide better velocity resolution but presumably poorer spatial resolution. There is currently no theory that will explicitly quantify the relationship between the waveform, the sensor locations and the phase-space resolution. This is left as an open problem.
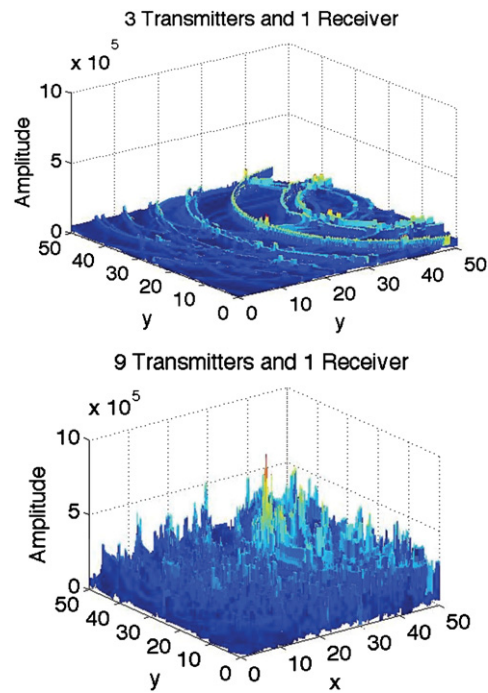
11

Figure 4. Stationary object PSF—perfect reflector, unknown paths. Top: three transmitters and one receiver. Bottom: nine transmitters and one receiver.
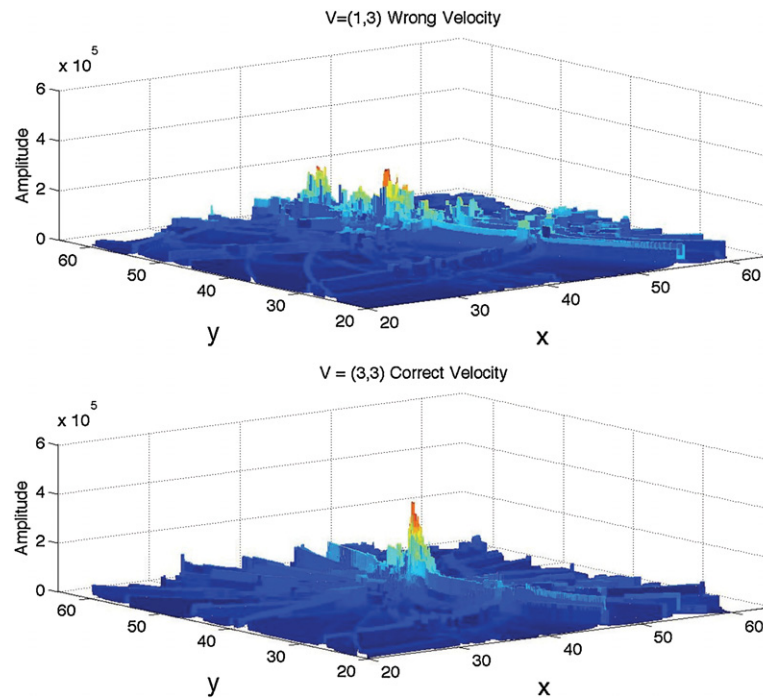

Figure 5. Spatial images of a moving object for different velocity hypotheses. This image is zoomed to show the spatial range [20 m, 60 m] $\times$ [20 m, 60 m]. Top: velocity $(1, 3) \times 10$ m s^{-1} (incorrect). Bottom: velocity $(3, 3) \times 10$ m s^{-1} (correct).

5. Conclusions

In this paper, we develop a method for forming a phase-space image of multiple moving objects in a known multipath environment from scattering data received at multiple sensors from multiple transmitters that could be transmitting different waveforms. The image is formed via a modified backprojection algorithm. In particular, the approach we take to arrive at the image formation algorithm involves developing a physics-based data model for the information we expect to receive at the receiving sensor and subsequently applying an adjoint to the data model in order to form the image. The resultant phase-space image is, in general, a six-dimensional image; in the case when objects and their motion are restricted to a plane, the phase-space image is four dimensional.

We characterize the performance of the imaging system by its PSF, for which we obtain an explicit formula. Numerical exploration of the PSF provides information about the degree to which the phase-space image contains information about position and velocity. In particular, from plots of the PSF, we are able to estimate the four- or six-dimensional resolution for the image and ascertain that multiple sensors do indeed improve the image resolution.

These results show that the modified backprojection algorithm developed in this paper is able to recover position and velocity information from moving-object scattering data collected in a known multiple-scattering environment. We also find that the PSF provides an insight into system design specifications, such as how many sensors are needed and what waveforms should be transmitted in order to produce a certain resolution image.

Much remains to be done. Our approach has assumed a simple, known multipath environment, perfect clock synchronization for coherent imaging and, in many cases, transmit waveforms that can be distinguished from one another by the receivers. We have also used a simple point-like target scattering model. Other imaging approaches, such as those incorporating sparsity and micro-Doppler techniques, remain to be explored.

References

[1] Borden B and Cheney M 2009 *Fundamentals of Radar Imaging* (Philadelphia, PA: SIAM)
[2] Cheney M and Bonneau R J 2004 Imaging that exploits multipath scattering from point scatterers *Inverse Problems* **20** 1691–711
[3] Cheney M and Borden B B 2008 Imaging moving targets from scattered waves *Inverse Problems* **24** 035005
[4] Gaburro R and Nolan C 2008 Microlocal analysis of synthetic aperture radar imaging in the presence of a vertical wall *J. Phys.: Conf. Ser.* **124** 012025
[5] Krishnan V and Yazici B 2011 Synthetic aperture radar imaging exploiting multiple scattering *Inverse Problems* **27** 055004

[6] Miranda A 2010 Imaging moving targets in a multipath environment with multiple sensors *Dissertation* Rensselaer Polytechnic Institute, USA

[7] Miranda A and Cheney M 2011 Imaging moving targets in a multi-path environment using multiple sensors *Int. Conf. on Electromagnetics in Advanced Applications (ICEAA)* pp 227–30

[8] Miranda A and Cheney M 2012 Imaging with waves bounced from a dispersive reflector *2012 IEEE Radar Conf. (RADAR)* pp 0156–60

[9] Nolan C J, Cheney M, Dowling T and Gaburro R 2006 Enhanced angular resolution from multiply scattered waves *Inverse Problems* **22** 1817–34

[10] Rihaczek A W 1969 *Principles of High Resolution Radar* (New York: McGraw-Hill)